LIMNOLOGY and OCEANOGRAPHY

ASLO

Limnol. Oceanogr. 9999, 2022, 1–18

doi: 10.1002/lno.12017

Impact of shallow-water hydrothermal seepage on benthic biogeochemical cycling, nutrient availability, and meiobenthic communities in a tropical coral reef

Anna Lichtschlag,[1*] **Ulrike Braeckman**,[2] **Katja Guilini**,[2] **Soeren Ahmerkamp**,[3] **Rachael H. James**,[4] **Dirk de Beer**[3]

[1]National Oceanography Centre, University of Southampton Waterfront Campus, Southampton, UK
[2]Marine Biology Research Group, Ghent University, Ghent, Belgium
[3]Max-Planck-Institute for Marine Microbiology, Bremen, Germany
[4]School of Ocean and Earth Science, National Oceanography Centre Southampton, University of Southampton Waterfront Campus, Southampton, UK

Abstract

We investigated the influence of high-CO_2 hydrothermal seepage on element cycling, early diagenetic processes, and meiobenthic communities in sediments of a coral reef in Papua New Guinea. Based on fluid flow velocities, determined from temperature gradients, and element concentrations, the solute fluxes from the seeps were estimated, showing that seepage through sediments can be a source of nutrients but also of potentially toxic elements to the reef ecosystem. The sediment pore waters consisted of up to 36% hydrothermal fluids, enriched in As, Si, Li, Mn, Fe, Rb, and Cs relative to ambient seawater. During their ascent to the seabed, the acidic fluids reacted with the sediments, leading to increases in total alkalinity, nutrients, and alkali elements in the fluids. Mixing of hydrothermal fluids with seawater within the sediments lead to precipitation of redox-reactive species, including Fe-oxides, but the sediment pore waters were still a source of trace metals to the water column. Presence of the low-pH fluids in the sediments resulted in dissolution of sedimentary carbonates and left behind finer-grained volcanoclastic sands containing As, Cr, and Ni in concentrations toxic to biota. These finer-grained sediments had a reduced permeability, reducing the rate of remineralization of organic matter. Benthic meiofauna and nematode abundance and functional diversity were relatively lower at sites with hydrothermal seepage through the sediment. As benthic and pelagic processes are tightly coupled, it is likely that the changes in benthic biogeochemical processes due to sediment acidification will also affect epibenthic and pelagic communities.

Tectonics are crucial for life as they return buried elements to the biosphere that would otherwise have become permanently unavailable for primary production and the rest of the food web. A major exchange pathway for returning elements to the Earth's surface is hydrothermal seepage, which supplies vast amounts of metals and other chemical species to the ocean (Resing et al. 2015). Deep-sea hydrothermal systems are hotspots of biodiversity as the reduced, chemical species in the advected fluids provide chemical energy for chemosynthetic communities in an otherwise sparsely inhabited environment (Jørgensen and Boetius 2007). The ecosystems of shallow-water hydrothermal seeps are more complex than their deep-sea counterparts as, in addition to the chemosynthetic organisms, typical shallow-water benthic communities are present, the latter being fuelled by photosynthesis and heterotrophic processing of organic matter transported into the sediments. Hence, CO_2-rich shallow-water hydrothermal seeps are natural analogues for studying the effects of ocean acidification on ecosystems and biogeochemistry (Aiuppa et al. 2021). Such seeps allow the study of the functioning of entire communities and specimens that have been exposed to low-pH conditions for long periods of time.

Large numbers of hydrothermal seeps are found in the "Ring of Fire" surrounding the Pacific Ocean; many of them are located in coral reefs and are ideal sites for studying the effects of ocean acidification on biota, as reefs harbor an enormous biodiversity and depend on calcification, a process that is challenged by low-pH conditions. Reef-building corals build large, permeable reef frameworks and host photosynthetic

*Correspondence: alic@noc.ac.uk

Additional Supporting Information may be found in the online version of this article.

algae, which add to the reef's primary productivity. In addition, microphytobenthos (Werner et al. 2008) and macrophytes make reefs unusually productive habitats, even though they usually inhabit oligotrophic waters. Reef sediments (Werner et al. 2006) and coral substrates (Rasheed et al. 2002) play crucial roles in the filtering and recycling of elements. Surface layers of reef sediments are often coarse-grained. In permeable, sandy surface-layers seawater often percolates up to several centimeters into the sediment, allowing increased microbial colonization and efficient uptake of organic matter and electron acceptors and release of the products of mineralization (Ahmerkamp et al. 2020). The released nutrients are subsequently available for the primary producers. This intensive recycling of organic material via permeable sediments contributes to the reef productivity and biodiversity.

Several studies have explored the impact of hydrothermal fluids on the geochemistry and ecology of shallow-water environments. Such sites were used as natural laboratories for ocean acidification and documented its effects on seagrass growth (Hall-Spencer et al. 2008), coral diversity (Fabricius et al. 2011), bacterial and metazoan community structure (Hassenrück et al. 2016; Smith et al. 2016; Molari et al. 2018), and bivalve populations (Martins et al. 2021). In addition to the acidifying effects of CO_2, input of toxic compounds from seeps can have strong effects on the ecosystem (Vizzini et al. 2013). Pore waters in hydrothermally influenced sediments often have low pH, high temperature, and high levels of reducing compounds (e.g., H_2S, Fe) compared to the overlying water column (Wenzhöfer et al. 2000). The advected hydrothermal fluids can also be enriched in Mn, As, Sb, Cr, Pb, Cd, Cu, and Zn and occasionally in nutrients (e.g., Si, NH_4; Sedwick and Stueben 1996, Pichler et al. 1999a). The composition of the upwelling hydrothermal fluids can be altered by mixing with oxic seawater below the seabed, precipitating constituents in the subsurface sediments or at the seawater-seabed interface (Pichler et al. 1999b).

This study assesses the effects of CO_2-rich, hydrothermal fluids on sediment and pore water biogeochemistry, and estimates the input of solutes associated with the seepage into the water column at a shallow-water (0.5–6 m) seep site in Papua New Guinea, where hydrothermal fluids are advected within a fringing coral reef. We determined the specific chemical signatures of the seep fluids to understand their origin, their formation process and the changes they undergo before they are released into the shallow-water sediments and water column. We studied meiofauna as a proxy for the influence of the seepage on the benthic ecosystem and discuss the effects of the hydrothermally influenced sediments and fluids on early diagenetic processes and the ecology of the coral reef ecosystem.

Methods

Study site

This study was conducted in the coastal waters of Normanby Island (9.49°S, 150.49°E), Papua New Guinea. The study site is located south of Upa-Upasina in the northwestern part of Normanby Island (Fig. 1b). Here, the tropical shallow-water shelf hosts a patchy distribution of individual corals, coral reef structures, macroalgae, and seagrass beds between open sediment patches. Submarine hydrothermal seepage occurs within this fringing coral reef at a water depth of 0.5–6 m, about 10–200 m from the shore. The tidal range at the sites is < 0.9 m with longshore currents between 2 and 4 cm s^{-1} and an average water residence time of ~ 2.5 h (Smith et al. 2016). Along the reef slope, hundreds of gas bubble streams emerge, covering an area of about 200 × 40 m, and fluids are advected through sediments and coral reef areas. Occasionally, more focused gas discharge sites are present. The emanating gas mainly consists of CO_2 (> 99% CO_2), with traces of methane, but no detectable H_2S (Fabricius et al. 2011). Whereas seeps can be defined as point sources of fluid release and vents of gas streams, both types occur simultaneously at all fluid flow sites at this location and are referred to as "seeps" in this paper. In May–June 2013 and April 2014 five of the largest, bubble streams-emitting sediment patches were sampled by scuba diving and snorkeling. These sites were named (from North to South) Seagrass (dominated by *Halophily ovalis*), Red Patch, Yellow Patch, Site 3.1, and Site 4 (Table 1; Fig. 1c). The sediments in the patches had a thickness of > 0.5 m and no sediment fluidization was observed. The seep sites were compared to a shallow "non-seepage" site (3 m average water depth, coarse-grained sediments), which did not show any visible seepage or temperature effects within the sediments. Previously recorded pH changes in the water column at this location were similar to other values along the coast (Fabricius et al. 2011); however, we cannot exclude that this site might occasionally be exposed to seawater containing a diluted hydrothermal component from the close-by seepage area. A deep "non-seepage" site (12 m average water depth, finer-grained sediments), was located approximately 500 m to the southeast of the seepage area, and was also not subject to advection of hydrothermal fluid through sediments.

Bottom water chemistry dynamics

Redox potential (Eh), pH, and tidal range (measured using pressure) were measured using RBR loggers (XR-420, RBR Ltd). The pH sensors were calibrated using NBS buffers (Mettler Toledo AG) at 29°C (i.e., in situ temperature) and values were converted to the total pH scale. The bottom water temperature was measured using HOBO Pendant temperature loggers tied to the RBR loggers. The loggers recorded the data 2–5 cm above the sediment surface for a continuous period of 5–11 d in May (23rd May to 2nd June at Site 3.1, Seagrass and Site 4) and June 2013 (4th June to 8th June at shallow "non-seepage" site and Red Patch). During these periods, the wave activity was low.

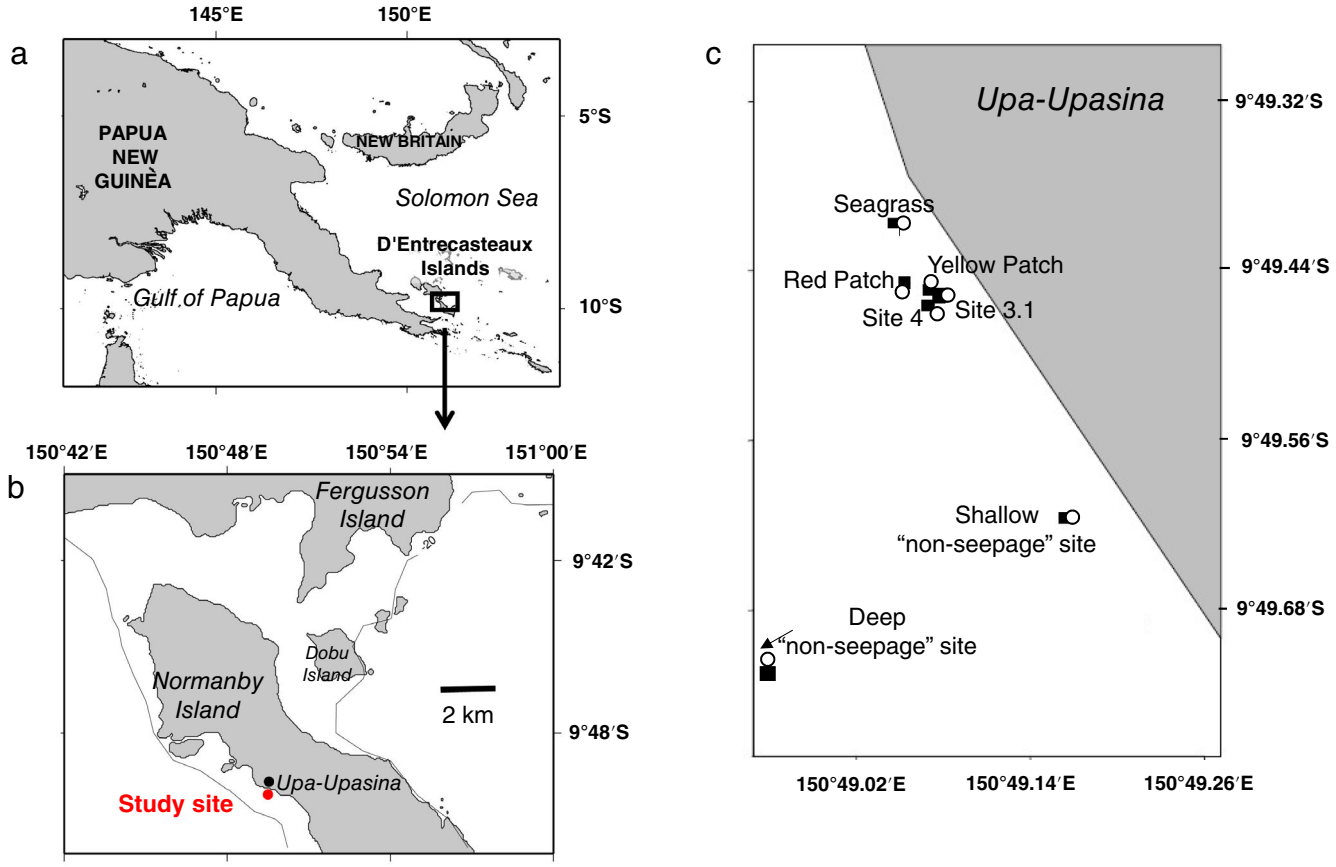

Fig. 1. **(a)** Location of the study site (D'Entrecasteaux Islands, Papua New Guinea; black box) and **(b)** offshore Normanby Island/Upa-Upasina (red dot); black lines indicate the 20 m isobaths; **(c)** schematic map of the sampling area; black squares represent sediment samples and white dots represent water column samples.

Element fluxes and turnover rates

High-resolution profiles of O_2, pH, and redox potential (Eh) in seep sediments

Microsensors for O_2 and redox potential were built, calibrated, and deployed as described previously (Revsbech 1989; de Beer et al. 2013). The oxygen microsensors, with a tip size of 150–300 μm, were calibrated in situ using the bottom water oxygen concentration and the anoxic pore water of deeper sediments. Redox potential microsensors were calibrated with standard redox buffers (191 mV and 468 mV, Omnilab-Laborzentrum GmbH & Co. KG). Needle-type microelectrodes (MI-407, 0.8 mm needle diameter, Microelectrodes, Inc.) were used for measuring pH (calibrated as described above). All sensors were mounted on a profiling lander, that is, a light frame and a titanium cylinder for the hardware, as described previously (de Beer et al. 2013), and the maximum distance between sensors was 11 cm. The profiling lander was programmed to obtain 10 cm deep vertical profiles in 250 μm steps during each deployment. Per investigated site 1–3 deployments (3× Seagrass; 3× Red Patch; 2× Yellow Patch; 2× Site 3.1, 2× Site 4; 1× shallow "non-seepage" site, and 1× deep "non-seepage" site) were successfully performed. Individual profiles are deposited in the PANGAEA database (https://doi.pangaea.de/10.1594/PANGAEA.857884).

Fluid upflow velocities

Temperature profiles were measured with commercially available temperature sensors (Pt1000, UST Umweltsensortechnik GmbH) that were also mounted on the profiling lander. Profiles were measured in the direct vicinity of gas streams (all sites except Seagrass) and > 1 m away from gas streams (all sites except Yellow Patch, where measurements in the vicinity of the gas streams were not possible). The temporal variability of pore water temperature was assessed by measuring 20 sequential profiles at the same location at Site 4 and the shallow "non-seepage" site.

Fluid upflow velocities v were derived from concave temperature profiles indicating upflow (Eq. 1) by applying a one-dimensional differential equation for heat transport through a saturated porous medium as previously used by Grevemeyer et al. (2006):

Table 1. Sampling sites with corresponding water depths, approximate sizes of the sediment patches, pH, and physical sediment properties; the area containing these seep sites (in total ~ 400 m^2) is approximately 8000 m^2. pH, porosity, and mean grain size are average values (± SD) over the core depth (complete data presented in Supporting Information Table S1); permeability is given for the upper 4 cm. At the Seagrass site, Red Patch (each 50 m^2 in area), and at Site 3.1 (100 m^2 in area) two cores were sampled and analyzed.

Site	Average water depth (m)*	Approximate size (m^2)	pH	Permeability ($\times 10^{-10}$ m^2)	Porosity	Mean grain size (phi)
Seagrass	3	~ 50	7.3 ± 0.3	0.19 (± 0.03)	0.4 ± 0.0	1.5 ± 1.6
Seagrass			n.d.	0.23 (± 0.05)	n.d.	n.d.
Red Patch	6	~ 50	6.5 ± 0.1	0.3 (± 0.0)	0.4 ± 0.1	1.7 ± 1.0
Red Patch			6.8 ± 0.3	n.d.	0.3 ± 0.0	0.9 ± 1.2
Yellow Patch	3	~ 100	6.9 ± 0.3	n.d.	0.4 ± 0.7	1.1 ± 0.7
Site 3.1	4	~ 100	7.1 ± 0.1	0.3 (± 0.01)	0.4 ± 0.0	2.4 ± 0.1
Site 3.1			6.4 ± 0.2	n.d.	0.4 ± 0.1	2.3 ± 0.0
Site 4	5	~ 100	6.1 ± 0.3	0.53 (± 0.03)	0.4 ± 0.0	1.6 ± 0.3
Shallow "non-seepage" site	3	—	7.8 ± 0.0	n.d.	0.3 ± 0.1	0.7 ± 0.8
Deep "non-seepage" site	12	—	7.9 ± 0.1	1.0 (± 0.13)	0.5 ± 0.0	1.0 ± 0.2

n.d., not determined.
*Tidal range < 0.9 m (Smith et al. 2016).

$$\frac{(T_z - T_0)}{(T_L - T_0)} = \frac{e^{\frac{\beta z}{L}} - 1}{e^{\beta} - 1}, \quad (1)$$

where T_z is the depth-dependent temperature, z is the depth, T_0 is the uppermost temperature measurement, T_L is the temperature at the deepest measured depth, and

$$\beta = \nu c_0 \rho_0 L \kappa^{-1}. \quad (2)$$

In Eq. 2, c_0 is the specific heat capacity of the fluid, L is the length between T_0 and T_L, ρ_0 is the density of the fluid, and κ is the thermal conductivity. Average pore water temperature and salinity were used to calculate c_0 (4008–4046 J kg^{-1} °C^{-1}), ρ_0 (1012–1020 kg m^{-3}), and κ (0.65–0.67 W m^{-1} °C^{-1}) using the R package "oce" (Kelly and Richards 2018). ν was calculated by fitting β to the temperature profiles, using temperature measurements from below 2 cm sediment depth, that is, excluding temperature changes due to bedform-induced pore water advection. Advection rates were defined as zero when pore water temperatures deviated by less than 0.5°C from the water column value.

The advective effluxes (J_{adv}) of elements into the water column were calculated from their pore water concentrations C and the modeled upflow velocities using:

$$J_{adv} = C\nu. \quad (3)$$

Potential oxygen consumption rates

Potential oxygen consumption rates in the permeable sediments were measured ex situ using the percolation method of de Beer et al. (2005) modified by Polerecky et al. (2005). Pore water oxygen concentrations were monitored using planar oxygen optodes designed for ratiometric read-out with an RGB camera (Larsen et al. 2011) with a sensing area of 50 × 10 mm that were glued vertically to the inside of an acrylic core liner (5 cm diameter). The planar optodes were calibrated in air-saturated and anoxic seawater. Sediments were sampled in these cores ($n = 3$ per site) and experiments were performed at in situ temperature (29°C). For this, bottom water was drained through the sediment cores using a peristaltic pump (30 mL min^{-1}) until the pore water was oxygenated. Upon stopping the percolation, the initial decrease of oxygen concentration over time was monitored in 1 mm depth intervals to a maximum depth of 4.5 cm. These potential oxygen consumption rates were then corrected for porosity. The areal oxygen uptake rates were obtained by integrating the potential oxygen consumption rates over the oxygen penetration depths measured in situ with the microsensors.

Sulfate reduction rates

Sulfate reduction rates were measured ex situ using a whole core injection method (Jørgensen 1978). Sediments were sampled with acrylic core liners (2.6 cm diameter) and pre-incubated in the dark at 29°C for 6 h before the start of the experiment (n = 2–4). Sediment cores were injected through silicone-filled ports at 1-cm depth intervals with 10–20 μL of $^{35}SO_4^{2-}$ (approximately 200 kBq), incubated for 6–7 h in the dark, sliced in 2-cm depth intervals, and fixed in an equal volume of 20% zinc acetate. Sulfate reduction rates were determined by single-step chromium distillation (Røy et al. 2014). Areal sulfate reduction rates were calculated by integrating the

volumetric sulfate reduction rates over the upper 10 cm of the sediment.

Sediments, pore water, and water column sampling

For geochemical analyses, three sediment cores (7 cm diameter) were taken next to each other at each site using 30 cm long acrylic core liners. One core was used to extract pore waters at 2 cm depth intervals with Rhizons (type: CSS, Rhizosphere Research Products, pore size < 0.2 μm, length 5 cm). Pore water subsamples were fixed with 10 μL of thermally distilled concentrated HNO_3 for cation analyses (0.5 mL), preserved with zinc acetate for analyses of sulfide and anions (0.3 mL), and fixed with saturated mercuric chloride in gastight glass vials with no headspace for analyses of dissolved inorganic carbon (DIC, 2 mL), total alkalinity (TA, 2 mL), and nutrients (1 mL). Multiple cores for pore water extraction were taken at Site 3.1 and Red Patch. The second core was used to sample the sediment solid phase at 2 cm intervals. Subsamples for porosity, grain size measurements and geochemical and mineralogical analyses were stored at 4°C. The pH of the sediment was determined in the porosity subsamples immediately after sampling with a pH electrode calibrated as described above. The sediments of the third core were sliced into 2 cm intervals and frozen at − 20°C for carbon and Fe(III) analyses.

Fluids from focused seeps emerging directly through gravely ground (Seagrass Seep) and through a sandy patch at Site 3.1 (Site 3.1 Seep) were sampled with syringes (100 mL) that were filled by inserting tubing into the seep opening. At Red Patch, seepage was more diffuse and the water column above the patch was sampled with a Niskin bottle that was closed manually ~ 20 cm above the seafloor. At both "non-seepage" sites the water column was sampled with a Niskin bottle close (< 0.5 m) to the seabed. Syringes and Niskin bottles were emptied into acid cleaned polyethylene bottles and acidified with thermally distilled concentrated HNO_3.

Sediment geochemistry and properties

The mineralogy of the sediments was determined on selected samples by X-ray diffraction on a Philips X'Pert Pro diffractometer, using CuKα radiation (35 kV, 40 mA) at angles from 2° to 76° with a step size of 0.02° and acquisition time of 1.2 s per step. Mineral phases were qualitatively identified with the Philips XPert software based on the PDF database from the JCPDS (Joint Committee on Powder Diffraction Standards).

The element compositions of selected samples from each site were determined by X-ray fluorescence (XRF, Philips MagiX-proWavelength dispersive XRF spectrometer, fitted with a 4 kW Rh end-window X-ray tube) on fused glass beads for major elements and on pressed powder pellets for minor elements.

Porosities were calculated from the loss of water after drying the sediment at 60°C, assuming a density of 2.6 g cm^{-3} for silicate-dominated sediments (i.e., seep sediments) and 2.7 g cm^{-3} for carbonate-dominated sediments (i.e., "non-seepage" sediments). Grain size was measured with a settling column. Sediment permeability of the upper 4 cm was measured with the falling-head method ($n = 3$).

Sediment samples ($n = 3$) for carbon analyses were freeze-dried, pulverized, and used for total carbon and organic carbon determination using an elemental analyzer (Euro EA 3000, EuroVector). Prior to measurement of organic carbon, the samples were decalcified in silver cups by addition of HCl. Total inorganic carbon was calculated as the difference between total carbon and organic carbon.

Reactive solid-phase Fe(III) was measured on frozen samples in the upper 8 cm of selected seep sediments and the shallow "non-seepage" site. The method is based on the extraction methods described by Kostka and Luther III (1994), using 0.2–0.5 g of frozen sediment and 10 mL of the respective extraction solution, but extraction steps were combined in a two times two-step extraction. Briefly, amorphous Fe oxides were first extracted with ascorbate solution and then Fe(III) from poorly crystalline Fe and magnetite was extracted with a degassed ammonium oxalate solution. In a 2nd subsample, most major Fe oxides were extracted with a citrate–acetate–dithionite solution and afterward the ready available Fe(III) bound to sheet silicates was extracted with 0.5 mol HCl. The Fe^{2+} and total Fe content of the leachate was determined using the Ferrozine method (Viollier et al. 2000). Fe(III) was calculated as the difference between total Fe and Fe^{2+}.

Pore water geochemistry

Pore water concentrations of Na, Mg, K, Si, B, Sr, Fe, and Mn were determined by inductively coupled plasma optical emission spectrometry (ICP-OES, Thermo Scientific Icap 6500 duo) and concentrations of Ca, Li, Ba, Rb, As, Co, Cs, and Ni by inductively coupled plasma mass spectrometry (ICP-MS; Thermo Scientific X-Series II) after diluting samples with 3% thermally distilled HNO_3. Measured concentrations of certified reference material for metals (CASS-4, Nearshore Seawater Reference Material) were mainly within ± 4% (Li, Mn, Co, Cs) and 10% (Ni, Ba) of the certified values, except for As, which had a larger discrepancy (± 19%). Instrument drift was assessed by addition of an internal standard (Re, In, and Be) during the ICP-MS measurements and analysis of one standard as an unknown every 10 samples for ICP-OES measurements. External reproducibility of the analyses was better than ± 6% for all elements.

Anions (SO_4 and Cl) were measured by ion chromatography (Dionex ICS 2500) with 9 mmol L^{-1} Na_2CO_3 as the eluent. Repeated analysis of International Association for the Physical Sciences of the Oceans (IAPSO) seawater standard and single anion standards showed a reproducibility of ± 0.5 mmol L^{-1} (2%) for SO_4 and ± 20 mmol L^{-1} (4%) for Cl.

TA was determined by titration against 0.002 mol L^{-1} HCl using a mixture of methyl red and methylene blue as an

indicator. Analyses were calibrated against IAPSO seawater. DIC was measured using an Apollo SciTech DIC analyzer (AS-C3), using a LI-COR CO_2/H_2O (LI-7000) infrared analyzer to detect CO_2 released from the sample after acidifying with 10% H_3PO_4; values might be underestimated due to outgassing during sampling. H_2S was determined photometrically according to Cline (1969). Phosphate and ammonium concentrations were measured with a QuAAtro nutrient analyzer. All biogeochemical pore water data are deposited in the Pangaea database (https://doi.pangaea.de/10.1594/PANGAEA.858033).

To determine the origin of the fluids, $^{87}Sr/^{86}Sr$ isotope ratios of selected pore water samples were determined by thermal ionization mass spectrometry (TIMS). Strontium was isolated from the rest of the sample matrix using an ion exchange resin. Briefly, a sample aliquot containing approximately 1 μg of Sr was loaded onto a column containing 50 μL of Sr-Spec resin. The matrix was eluted with 3 mol L^{-1} HNO_3 and the Sr fraction was then collected in MilliQ water. The purified Sr sample was dried and loaded onto a single Ta filament using a Ta activator solution and $^{87}Sr/^{86}Sr$ ratios were measured with a Thermo Fisher Triton Plus TIMS using a static routine with amplifier rotation and a ^{88}Sr beam intensity of 2 V for 300 ratios. Results were normalized to a $^{86}Sr/^{88}Sr$ ratio of 0.1194 using an exponential correction. The standard error ($\pm$ 2SE) of an individual analysis was < 13 ppm. The long-term reproducibility of analyses of the NIST 987 standard was 0.710243 $\pm$ 0.000021 ($\pm$ 2SE).

Meiofauna abundance

Sediment samples for meiofauna analysis were collected at the shallow "non-seepage" site, Red Patch, Site 3.1, and Site 4 using core liners with an inner diameter of 5 cm, which were precut in 2 cm steps and taped ($n = 3$). The sediments were vertically sectioned in 2 cm slices, down to a maximum depth of 8 cm. All sample sections were preserved in a 4% seawater-buffered formalin solution. Meiofauna were extracted from the samples through triple density centrifugation with the colloidal silica polymer LUDOX TM 40 (Heip et al. 1985) and rinsed with freshwater on stacked 1-mm and 32-μm mesh sieves. The fraction retained on the 32-μm mesh sieve was preserved in 4% Li_2CO_3-buffered formalin and stained with Rose Bengal. All metazoan meiobenthic organisms were classified at higher taxon level and counted under a stereoscopic microscope (Leica MZ 8, 16×5×). Nematodes, 50 per sediment layer (where possible) were randomly handpicked with a fine needle, transferred to glycerine (De Grisse I, II, and III) (Seinhorst 1959), mounted on glass slides, identified to genus level based on the Nemys website (Guilini et al. 2016), and allocated to functional feeding groups based on Wieser (1953) (selective deposit feeders—1A, non-selective deposit feeders—1B, epistratum feeders—2A, and predators/scavengers—2B).

To test for differences between sites in meiofauna and nematode densities, a one-way ANOVA was performed. When significant between-site differences were observed, a Tukey HSD post hoc comparison test (at $\alpha = 0.05$) was applied to identify the sites responsible for the observed differences. Patterns in nematode community composition were explored with non-metric dimensional scaling based on a Bray–Curtis similarity matrix and between-site differences were tested with a permutational permanova, both using the vegan package (Oksanen et al. 2019). All statistical analyses were performed using the free statistical environment R (v.4.0.2) (R Core Team 2020).

Results

Seepage dynamics

The pH, temperature, and Eh of the bottom water varied with the tides, with pH and Eh minima and temperature maxima correlating with low tide (Fig. 2). Thus, seepage was enhanced at low tide. At the shallow "non-seepage" site, pH variations were very modest (< 0.2 units), but temperature and Eh were variable, showing that the water column might have been influenced by seepage, although the temperature variability might also come from natural changes in the thermocline. The relative changes in pH, Eh, and temperature were different between the different sites; largest changes in pH were recorded at the Seagrass site and highest shifts in Eh were observed at the Red Patch.

Element fluxes and turnover rates

In situ measurements of O_2, pH, and Eh

The in situ profiles of O_2, pH, and Eh in the overlying water column and the uppermost 8 cm of the sediments at the seep sites were characterized by low pH and Eh, and rapid oxygen depletion below the seabed (Fig. 3). The oxygen penetration depth was lower at the seep sites compared to the shallow "non-seepage" site, either due to enhanced oxygen consumption or upward advective flow of anoxic seep fluids. In all seep sites the pore water pH reached values of < 6–7. The redox potential showed a sharp decline just below the sediment surface and often decreased to negative values a few centimeters below the seabed, indicating reduced conditions close to the seabed. The profiles in the shallow "non-seepage" site showed no influence of seepage, with a pore water pH above 7.5 and an Eh close to bottom water levels.

Potential oxygen consumption and sulfate reduction rates

Seepage lead to elevated potential volumetric oxygen consumption rates (Supporting Information Fig. S1). The rates at the shallow "non-seepage" sites were low and constant with depth, while rates at seep sites were 2–5 times higher and often increased with depth. Although seep sediments have enhanced consumption rates, the areal oxygen uptake rates, calculated from the potential volumetric rates multiplied by the oxygen penetration depth (Fig. 4b), are mostly lower than at the shallow "non-seepage" site (Fig. 4c), due to the reduced oxygen penetration depth.

In all sediments, the areal sulfate reduction rates were 1–2 orders of magnitude lower than areal oxygen consumption rates (Fig. 4d; Supporting Information Fig. S2). As sulfate

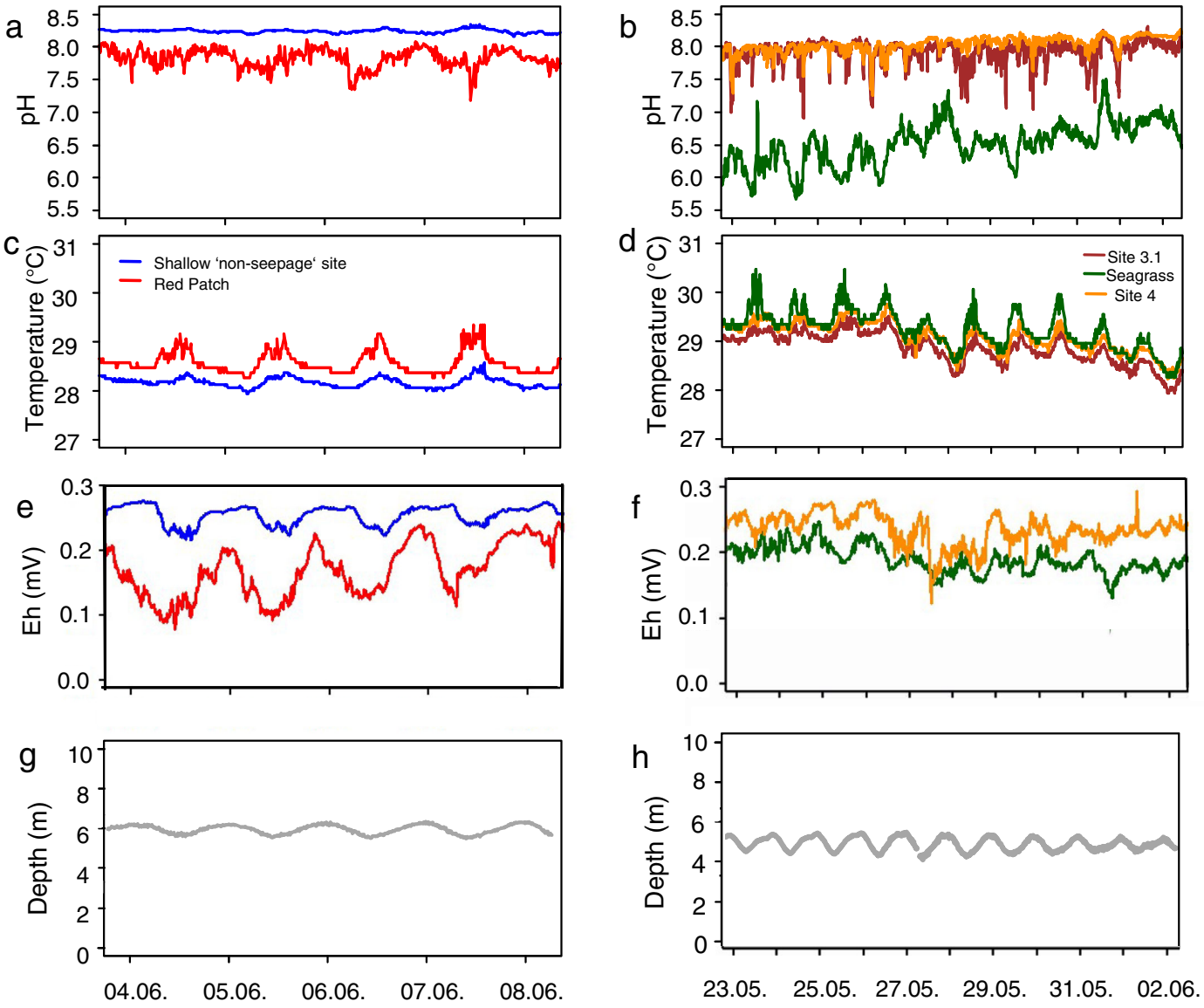

Fig. 2. Bottom water pH (**a**,**b**), temperature (**c**,**d**), and Eh (**e**,**f**) at the investigated sites. Note that seep sites have a lower pH and Eh than the shallow "non-seepage" site; variations in depth (tidal range) at the Red Patch (g) and Site 4 (h) show the influence of tides.

reduction might have occurred below our sampling depths, the rates may be underestimated. Sediments at seep sites had much lower sulfate reduction rates (0–1.1 mmol m^{-2} d^{-1}) than at the shallow "non-seepage" sites (1.9–2.6 mmol m^{-2} d^{-1}, (Fig. 4d), except for the Seagrass site that had relatively high sulfate reduction rates (up to 6.6 mmol m^{-2} d^{-1}). In summary, rates of organic matter mineralization were decreased by seepage and elevated in seagrass areas.

Fluid upflow velocities and element effluxes

Measured temperature profiles and modeled fluid upflow velocities are presented in Fig. 5. In the seep sites the temperature rapidly increased with depth (0.3–1.2°C cm^{-1}). "Non-seepage" sites showed no temperature increase, thus upflow velocities were 0. Within the seepage area, the fluid upflow velocities varied temporally and spatially, which is indicated by the range in velocities given in Table 2.

Fluid upflow velocities and element concentrations within seep sediments were patchy as there are complex mixing processes proceeding in the sediments, including the one-directional seepage of fluids from the subsurface and the formation of convection cells (Wenzhöfer et al. 2000; Haeckel et al. 2007). In addition, the tide will influence fluid outflow velocities. Other uncertainties in calculating net releases from sediments are that locations and intensities of bubble streams can vary with time (Flohr et al. 2021) and some of the released

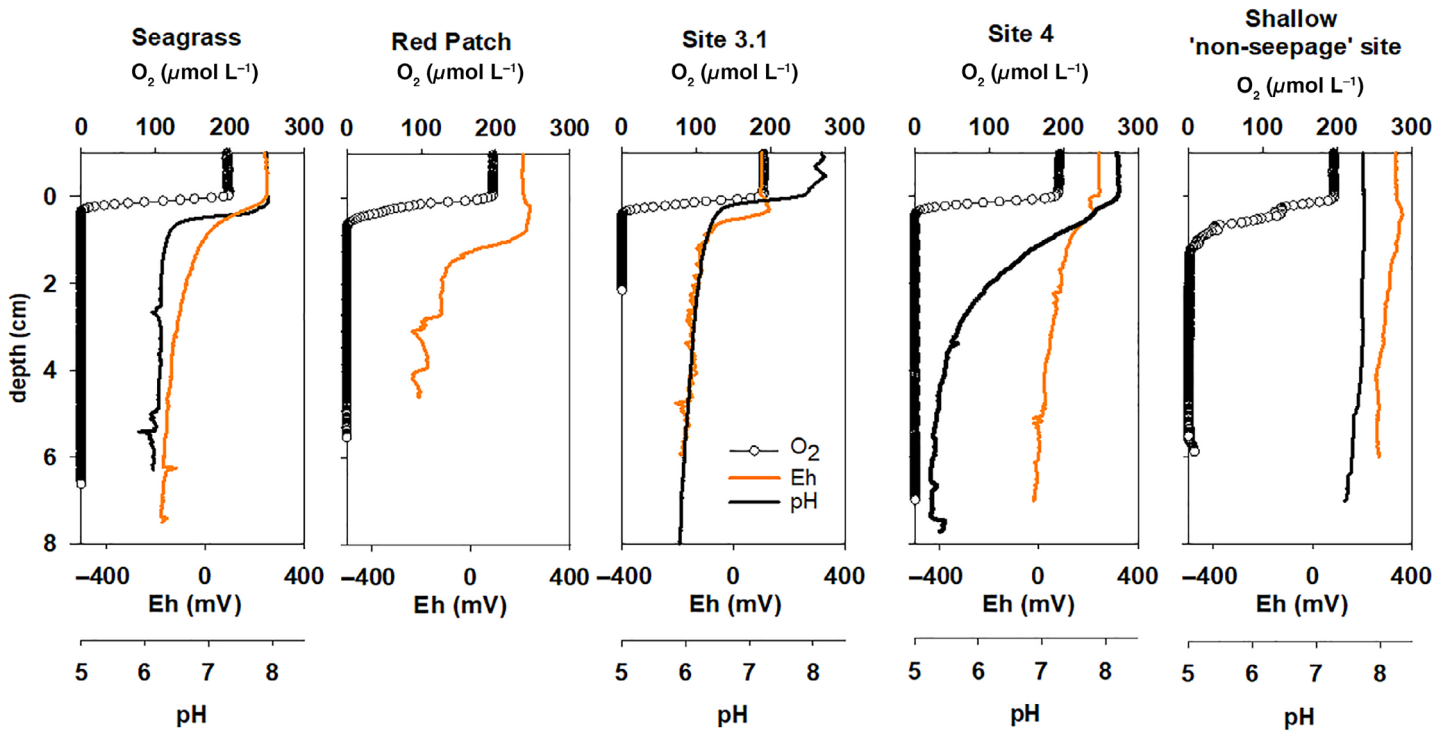

Fig. 3. Exemplarily in situ microsensor profiles of oxygen (O_2, white dots), redox potential (Eh, orange line), and pH (black line). No in situ pH profile was measured at Red Patch, but pH analyses of pore water samples (Supporting Information Table S1) indicated that the pH was decreased within the sediments.

fluids might be entrained back into the sediment through the convection of the fluid. To accommodate the fact that there will be areas with higher fluxes (e.g., close to fluid release points) and areas with low or no fluxes (e.g., ingression of seawater through convection cells), a range of element effluxes for each site are presented in Table 2. The fluxes of the different elements varied hugely. Of the biologically important elements, N and P effluxes were high, but also the lower fluxes of trace metals (Ni, Fe, Co, As) may have significant biological impacts (Table 2).

Composition and physical properties of sediments

Sediments at most seep and "non-seepage" sites were dominated by sand (72–95%) with a typical porosity of about 0.3–0.5 (Table 1, Supporting Information Table S1). Sediments from the "non-seepage" sites consisted of coarse calcite; the seep sediments were dominated by much finer silicate material. The shallow 'non-seepage' site was highly permeable (1×10^{-10} m^2), while the permeabilities in seep sediments were 2–5 times lower (Table 1). All sediments had low organic carbon content (Fig. 4a), with the highest values found at the Seagrass and the "non-seepage" sites. Mineralogical analyses showed that seep sediments were rich in quartz, plagioclase, K-feldspar, and antigorite (a serpentine mineral formed under low-grade metamorphosis). Both "non-seepage" sites contained Mg-rich calcite and aragonite. XRD and sequential extractions confirmed that amorphous iron oxides were present at all seep sites, with especially high levels of reactive iron found at Red Patch (Supporting Information Fig. S3).

The major element composition was similar in all seep sites (Supporting Information Table S2). When calculating the relative abundances of major elements in both "non-seepage" sites on a carbonate-free basis, the distribution of major elements was similar in "non-seepage" and seep sites (Supporting Information Fig. S4). This indicates that the silicate sands found at the seep sites had been stripped of carbonate by acid seepage. An exception was Red Patch, which had about 2–3 times higher content of Fe, Mg, and P (Supporting Information Table S2). This coincided with highest contents of As, Cr, Co, and Ni, indicating a volcanic origin. Sediments at Site 3.1 and the Seagrass site were enriched in Cr compared to the "non-seepage" sites, but not in As or Co. Site 4 was only enriched in Ni compared to the "non-seepage" sites (Table 3).

Chemical composition of pore waters and focused seep fluids

The pore water composition in seep sediments differed profoundly from that of "non-seepage" sediments (Fig. 6; Supporting Information Table S3; Fig. S5). The seep site pore waters were enriched in As, Li, Si, Rb, Sr, Ba, and Ca, were depleted in Na, Mg, and K and had elevated TA and DIC concentrations compared to the "non-seepage" sites. Strongest

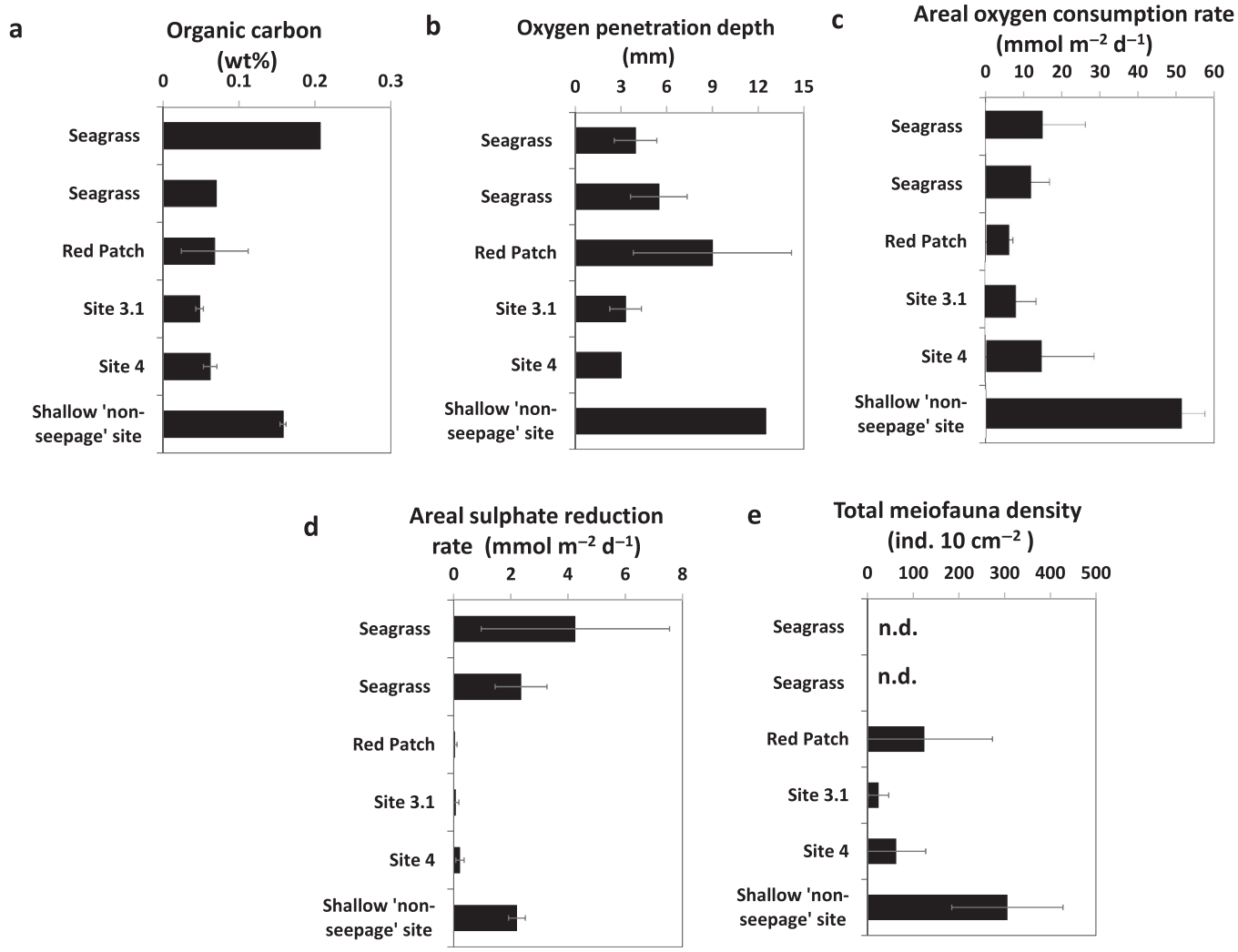

Fig. 4. (**a**) Organic carbon content in the upper 4 cm, (**b**) oxygen penetration depth, (**c**) areal oxygen consumption rates (integrated over the oxygen penetration depth), (**d**) areal sulfate reduction rates (integrated over 10 cm), and (**e**) total meiofauna density from the upper 4 cm of sediments from the seeps and shallow "non-seepage" sites; n.d. = not determined.

enrichments were found at Site 3.1 and Red Patch, especially in As. Seep pore waters were depleted in SO_4 and Cl, with lowest values again at Site 3.1 and Red Patch.

The geochemical signature of the seep fluids emerging through gravely ground (focused seep fluids), was similar to that of the seep pore waters, that is, depleted in Mg, Cl, and SO_4 and enriched in Li, redox-reactive elements (including Fe and Mn), and NH_4 compared to ambient seawater (Supporting Information Table S4). No sulfide was detected in any of the fluids.

The $^{87}Sr/^{86}Sr$ isotope ratio of the pore water from the "non-seepage" site was 0.709132, close to modern seawater (~ 0.7091; Mokadem et al. 2015). Pore waters from Site 4 also had $^{87}Sr/^{86}Sr$ ratios (0.709143) close to seawater. The $^{87}Sr/^{86}Sr$ isotope ratios of pore waters from the other seep sites varied between 0.705032 and 0.705062, with lowest values measured in the 3.1 focused seep fluids (Supporting Information Table S5), indicating reaction of the fluid in the subsurface.

Composition of the hydrothermal fluid endmember

The SO_4 concentration of the pore water was used to calculate the relative contributions of the original, undiluted hydrothermal fluid (i.e., the fluid endmember) to the pore waters and to determine the fluid endmember composition. In principle, also Mg could be used for this calculation (as hydrothermal fluids are Mg- and SO_4-free due to the quantitative removal of both compounds from seawater during high-temperature seawater–rock interactions; Bischoff and Seyfried 1978); however, in sediment-hosted hydrothermal systems, Mg can be added to the fluid as it percolates through the sediments (Sedwick and Stueben 1996). The decrease in

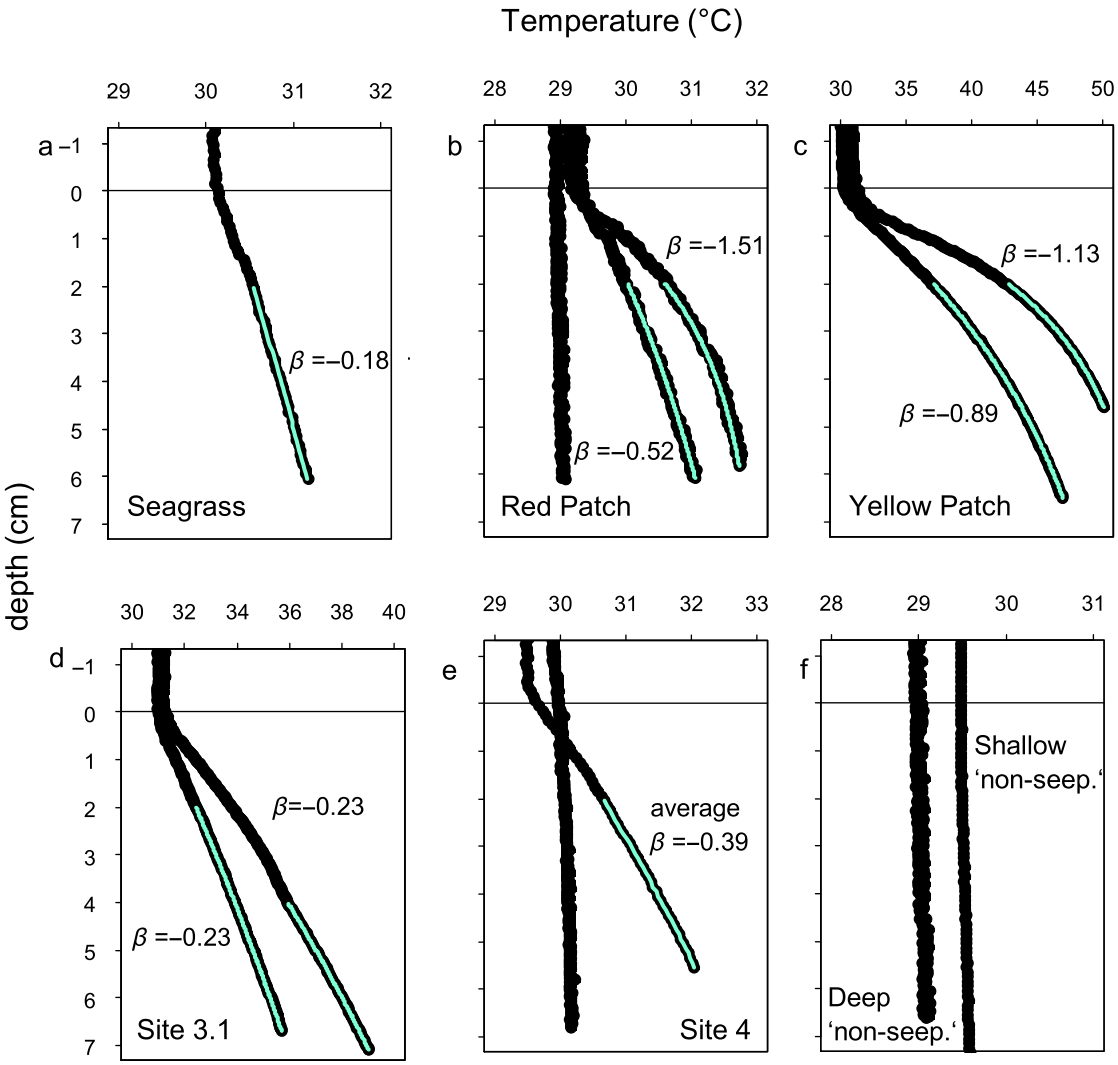

Fig. 5. (**a**–**e**) Fluid upflow is indicated by the concave shape of the temperature profiles (black line). Fluid upflow velocities were calculated from fitting β (Eq. 2) to the temperature profiles (cyan). In both "non-seepage" sites (**f**), and one profile from Red Patch (**b**) and Site 4 (**e**), constant temperature profiles suggest no upflow. For the concave profile at Site 4 and the shallow "non-seepage" site averages of 20 continuously measured profiles are shown. Note the different temperature scales.

sulfate concentration could also come from sulfate reduction in the sediments; however, the measured sulfate reduction rates were very low in the seep sediments (Fig. 4). The calculations showed that the pore waters consisted of up to 36% hydrothermal fluid (Table 2). Calculated endmember Cl, Na, Si, and Mg concentrations were similar to those reported for other shallow-water seeps, while concentrations of Ca, Li, B, Sr, and PO_4 were higher (Supporting Information Table S6).

Meiofauna and nematode communities

All meiofauna species (nematodes, copepods, amphipods, nauplius larvae, and tardigrades) were strongly reduced by seepage (Supporting Information Fig. S6) and the community composition was also strongly influenced by seepage. Some species were actually favoring from seepage. Meiofauna and nematodes were most abundant in the upper two centimeters of the sediment, and their abundance decreased with increasing sediment depth. At the shallow "non-seepage" site the decrease in abundance with depth was gradual, but it was much steeper at the seep sites, falling by 85–87% between 0–2 and 2–4 cm depth, again showing that the seep sites repel meiofauna.

Although rather low in abundance, the nematode community was quite diverse, with 48 genera encountered in the upper 4 cm of all sites, belonging to 17 families. Nematode total density was higher at the shallow "non-seepage" site (661 ± 87 ind. $10\,cm^{-2}$) than at the seep sites (141 ± 128,

Table 2. Percentage hydrothermal fluid component in the pore waters, ranges of fluid upflow velocities and of effluxes of selected elements from the seep sites. Fluxes are calculated by multiplying the fluid upflow velocities with the lowest and highest concentrations of the specific elements in the pore water (Supporting Information Table S3).

		Seagrass	Red Patch	Yellow Patch	Site 3.1	Site 4
% Hydrothermal fluid component		—	18–32%	—	32–36%	7%
Fluid upflow velocities (m d−1)		0.12	0.18–0.52	0.25–0.59	0.09–0.10	0.09–0.21
Efflux (mmol m^2 d^{-1})	Mg	2800–3300	3600–11,700	6000–15,700	1800–2400	2100–5400
	Ca	610–680	950–3150	1210–3230	410–670	420–1020
	K	560–700	690–2250	1210–3090	360–490	400–1080
	Li	1.5–2	14–71	4–9	1–14	1–3
	Si	4–11	73–367	21–68	3–72	4–28
	B	20–25	43–175	47–119	14–34	16–42
	Sr	4–5	22–84	10–27	3–16	3–8
	Fe	0–1	1–29	3–25	0–5	17–50
Efflux (μmol m^2 d^{-1})	NH_4	960–3950	3800–16,850	1050–2480	330–4090	1210–4250
	PO_4	60–280	90–490	120–280	0–90	40–190
	Rb	60–90	520–1880	190–850	60–430	50–120
	Ba	6–11	51–244	23–83	4–64	4–9
	Mn	110–400	590–3420	120–1100	0–1010	80–280
	As	50–60	20–1020	60–590	10–130	50–130
	Co	0–2	0–12	6–19	0–19	3–14
	Cs	0–3	0–370	19–123	4–85	0–1
	Mo	5–12	1–27	9–64	0.3–7	2–4
	Ni	6–34	8–171	117–276	4–28	57–443

55 ± 49 and 11 ± 8 ind. 10 cm^{-2} in Red Patch and Site 4 and Site 3.1, respectively; one-way ANOVA $F_{3,8} = 41.01$, $p < 0.001$). As shown in Fig. 7, the nematode community composition differed significantly between the four sites (permanova pseudo-$F_{3,8} = 3.48$, $p = 0.001$), with locations explaining nearly 60% of the variability in community composition (permanova R^2 for "site" = 0.57). The most abundant genus *Odontophora* at the shallow "non-seepage" site (20%) occurred in Red Patch and Site 4 as well in comparable contributions (Supporting Information Table S7), but much lower absolute numbers. The Epsilonematid genera *Epsilonema*, *Perepsilonema* and the Draconematid genus *Dracograllus* jointly contributed 14–20% to the shallow "non-seepage" site community, but were virtually absent at the seep sites (< 0.2%). Seep sites in turn, were primarily inhabited by Cyatholaimidae (*Paracantonchus* and *Paradesmodora*) and Oncholaimidae such as the genus *Oncholaimus* (up to 37% and 32% in Site 3.1, respectively), Chromadoridae (*Hypodontholaimus* and *Dichromadora*, up to 58% in Red Patch) and Desmodoridae (mainly *Spirinia*; 52% in Site 4; Fig. 7; Supporting Information Table S7). Functional diversity in terms of feeding types changed dramatically from the shallow "non-seepage" site to the seep sites: selective deposit feeding nematodes were virtually absent in the seep sites, whereas the contribution of epistrate feeders (i.e., nematodes feeding on [benthic] diatoms), predators, and scavengers increased (Supporting Information Fig. S7).

Discussion

Origin and evolution of fluids in Normanby Island sediments

The fluids advected through the sediments at the Normanby Island seeps have a hydrothermal signature, with high concentrations of dissolved trace metals and Si, Li, Ca, B, Rb, and Sr and reduced concentrations of Mg, Cl, and SO_4 relative to seawater (Supporting Information Table S3).

Plots of element concentrations vs. SO_4 (Fig. 6) and the low standard deviations of the calculated hydrothermal fluid endmember for conservative elements (Supporting Information Table S6) indicate a single hydrothermal fluid source. $^{87}Sr/^{86}Sr$ isotopic ratios of the pore waters and seep fluids extrapolate to a value of ~ 0.7039 in the endmember fluid, which is slightly lower than the value of volcanic rocks in the vicinity of the sampling site (dacites from Normanby Island: $^{87}Sr/^{86}Sr = 0.70436$, Smith and Compston 1982). Mass balance considerations indicate that the geochemical signature of the seep fluids cannot be entirely explained by simple mixing between the hydrothermal fluid and seawater endmembers, but rather the seep fluids have reacted with the sediments as they are advected toward the sediment surface. Element/Cl ratios of the more mobile alkali elements (Li, Rb, Cs) and Sr, B, and Si are relatively high compared to typical vent fluids from sediment-free hydrothermal systems (Von Damm 2001, Supporting Information Table S6), which is indicative of

Table 3. Minor element composition of selected sediment samples from seep and "non-seepage" sites compared to sediment quality guidelines for heavy metal effects on benthic fauna. Metals that exceed the levels where effects are frequently found are shown in bold.

									Sediment quality guidelines (Long et al. 1995)		
Site (depth)	Seagrass (19 cm)	Red Patch (11 cm)	Red Patch (9 cm)	Site 3.1 (19 cm)	Site 3.1 (17 cm)	Site 4 (13 cm)	Shallow "non-seepage" (13 cm)	Deep "non-seepage" (11 cm)	Rarely associated with effects	Occasionally associated with effects	Frequently associated with effect
As (ppm)	10	**424**	**507**	5	18	6	b.d.	b.d.	< 8.2	8.2–70	> 70
Ba (ppm)	692	611	653	764	761	772	612	543	n.a.	n.a.	n.a.
Ce (ppm)	53	68	73	51	52	42	33	37	n.a.	n.a.	n.a.
Co (ppm)	7	16	18	5	6	6	4	4	n.a.	n.a.	n.a.
Cr (ppm)	**2306**	**1180**	**3411**	**1913**	**912**	217	171	290	< 81	81–370	> 370
Cu (ppm)	b.d.	b.d.	b.d.	b.d.	b.d.	b.d.	9	6	< 34	34–270	> 270
Mo (ppm)	b.d.	5	3	b.d.	b.d.	b.d.	b.d.	b.d.	n.a.	n.a.	n.a.
Nb (ppm)	4	5	6	5	4	5	4	3	n.a.	n.a.	n.a.
Ni (ppm)	**87**	**146**	**142**	**59**	**55**	**82**	31	30	< 20.9	20.9–51.6	> 51.6
Pb (ppm)	10	11	13	12	10	12	8	7	< 46.7	46.7–218	> 218
Rb (ppm)	62	63	55	77	67	75	48	39	n.a.	n.a.	n.a.
Sr (ppm)	421	218	230	258	217	251	1941	2246	n.a.	n.a.	n.a.
Zn (ppm)	37	35	56	36	29	32	24	23	< 150 0	150–410	> 410
Zr (ppm)	134	157	172	157	133	174	61	35	n.a.	n.a.	n.a.

b.d., below detection; n.a., not analyzed.

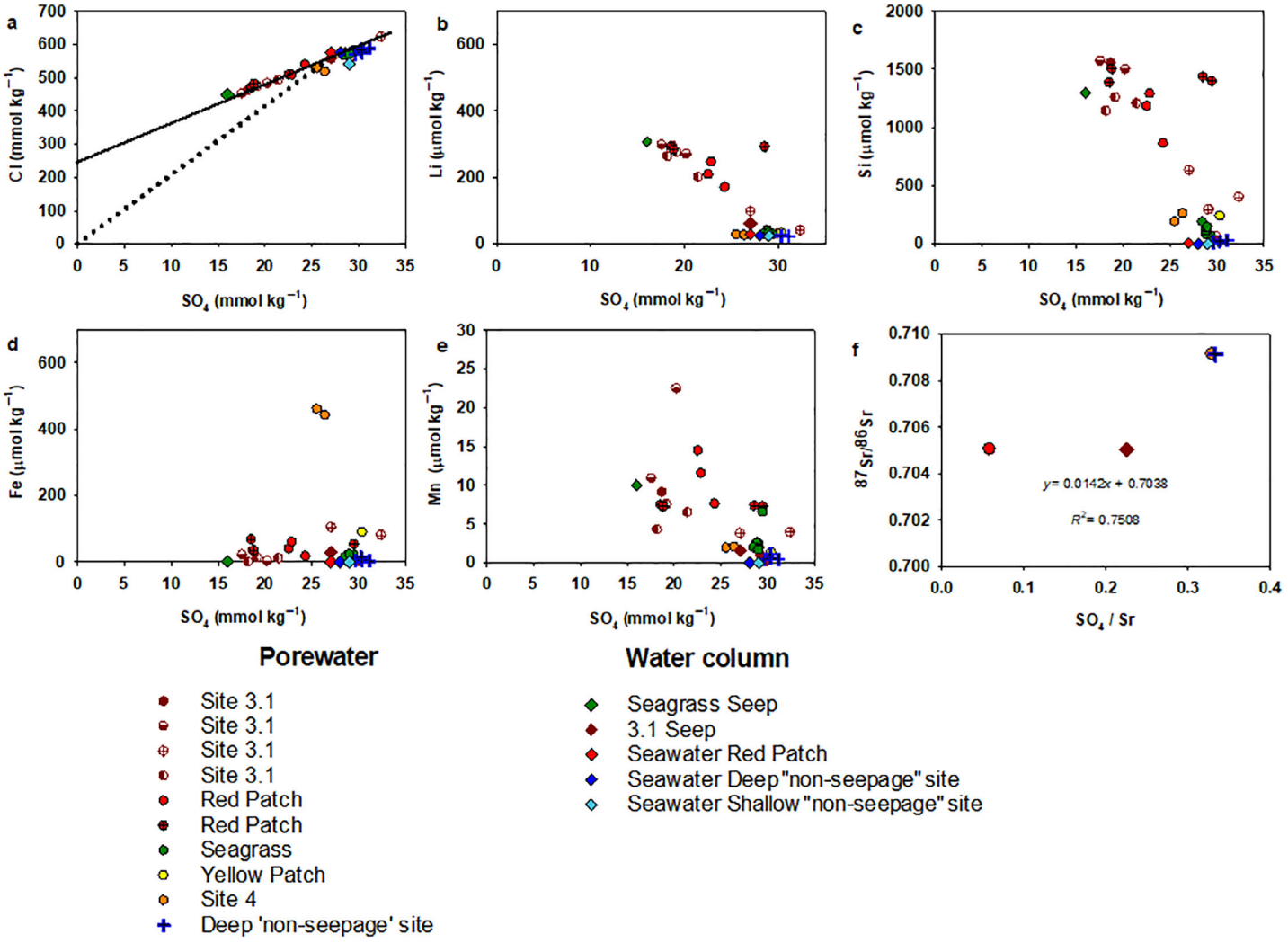

Fig. 6. Correlations between SO_4 and Cl, Li, Si, Fe, Mn, and correlation of SO_4/Sr and $^{87}Sr/^{86}$ Sr. In (**a**) the solid black line indicates the correlation and the dashed line indicates seawater Cl/SO_4 extrapolation.

leaching from the overlying sediments at moderate temperatures (James et al. 2003). Weathering of carbonates is further indicated by the relatively high TA concentrations (up to 20 mmol L^{-1}, Supporting Information Table S3) in seep fluids. Similarly enhanced TA values coupled with high alkali element/Cl ratios have been reported, for example, in CO_2-rich hydrothermal fluids in the Okinawa Trough (de Beer et al. 2013). Chloride concentrations in pore waters were depleted compared to seawater and the Cl concentration of the hydrothermal fluid endmember is about 50% that of seawater (~ 250 mmol kg^{-1}, Fig. 6a). Low Cl concentrations may be due to phase separation in the subseafloor (Butterfield et al. 1990), or in the case of shallow-water hydrothermal seeps, due to the ingression of freshwater (Pichler et al. 1999a).

The presence of NH_4 (Supporting Information Table S3) in the pore waters of the seep sediments could be indicative of diagenetic or thermogenic organic matter degradation by the percolating CO_2-rich fluids (e.g., Sedwick and Stueben 1996). PO_4 is usually depleted in hydrothermal fluids (Wheat et al. 1996); however, in our study sites some PO_4 is present, possibly due to iron reduction in surface sediments with release of P absorbed to the Fe-oxides (Poulton and Canfield 2006).

Concentrations of redox-reactive metals in the pore waters and seep fluids are relatively low (Supporting Information Table S3) compared to typical hydrothermal fluids (Von Damm 2001), and there is little correlation between metal concentrations and concentrations of SO_4 (Fig. 6). Mixing between hydrothermal fluids and oxic, pH-neutral seawater likely results in precipitation of metal (oxyhydr)oxides (Pichler et al. 1999b). At seeps, mixing with seawater can occur through the formation of centimeter- to meter-sized convection cells below the seabed (Wenzhöfer et al. 2000;

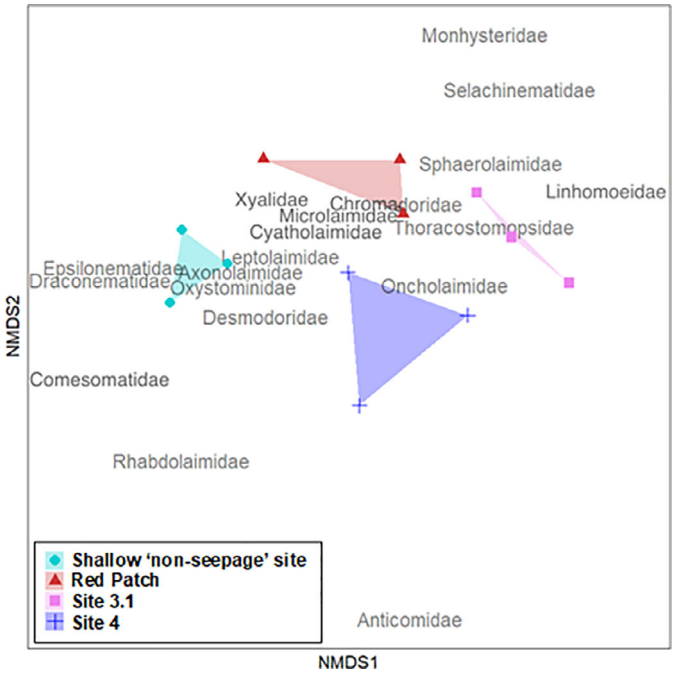

Fig. 7. Nonmetric multidimensional scaling plot (stress = 0.09) of the nematode community in the 0–4 cm sediment of the shallow "non-seepage" and seep sites ($n = 3$).

Haeckel et al. 2007). The temperature distributions, the variability of the microsensor profiles and the high variability in fluid flow rates (Fig. 3; Table 2) indicate that conditions for metal precipitation within seabed sediments are met. Moreover, carbonate dissolution will raise the pH of the pore waters, which can also promote metal precipitation. In support of this, highest concentrations of metals in pore waters (Fe, Mn, Ni, Co) correlate with lowest pH conditions in the sediments (Site 4, Supporting Information Fig. S5).

Ecological consequences of advection of hydrothermal fluids

As discussed above, the chemical composition of the seep fluids reflects advection of hydrothermal fluids, reactions between fluids and sediments and mixing with seawater in the shallow subsurface. As a result, warm, low-pH fluids are present in the coral reef sediments. These fluids contain no dissolved sulfide and are enriched in dissolved metals and some nutrients compared to ambient seawater. Input of these solutes into the near-surface sediment and the overlying water column can have an impact on the local coral reef ecosystem.

Ecotoxicological effects

Accumulations of hydrothermally derived metals in sediments of shallow-water seeps often reach levels that could have adverse effects on biology (Vizzini et al. 2013). Normanby Island consists of serpentinized ultramafic rocks, gneiss with mafic dikes, volcanic rocks and granodiorites (Little et al., 2007). The composition of sediments from "non-seepage" sites with the carbonates removed, was similar to that of the seep sites (Supporting Information Fig. S4), hence it is the dissolution of carbonates by the low-pH fluids that has led to the accumulation of the metal-rich volcanoclastic sand. At high concentrations, metals contained in sediments can be toxic to infauna and to assess the potential for ecotoxicological effects, the sediment metal contents are compared to quality guidelines for marine sediments in Table 3. In sediments from all seep sites Cr and Ni contents were at levels that are frequently associated with biological effects. It is notable that at Red Patch, As, Cr, and Ni contents were one order of magnitude higher than the threshold for frequently negative effects on fauna (Long et al. 1995, Table 3). This can be related to the precipitation of iron oxides at this site; however, it is not clear why more iron and other redox-sensitive elements precipitated here compared to the other sites, but similar patchy phenomena have been observed before (Pichler et al. 1999b). Thus, in addition to high-CO_2, low-pH, and elevated temperature, the high heavy metal contents of the sediments could be a key factor for explaining the drastic reduction in sediment meiofauna in the seep sites (Fig. 4e), as also suggested for the bacterial community at the same seeps (Hassenrück et al. 2016). The seep sediments also constitute a less attractive hiding place for demersal plankton, which reside in the sediments at night and were notably reduced at the seep sites (Smith et al. 2016).

Remineralization and changes in community structure in seep sediments

Sediments are important for the remineralization of organic matter in coral reef environments, with early diagenetic processes typically dominated by oxygen respiration and sulfate reduction (Werner et al. 2006). We found a clear reduction in oxygen consumption rates in most seep sites. A reduced supply of oxygen is visible from the lower oxygen penetration at the seep sites (Figs. 3, 4) and the presence of reduced compounds in the advected fluids will further reduce pore water oxygen levels. The reduction in grain size and the lower permeability of the seep sediments, caused by carbonate dissolution, will also reduce the advective exchange between pore water and bottom water and hence the supply of organic matter and oxygen to surface sediments (Huettel et al. 2007). This reduced availability of oxygen and carbon can limit aerobic respiration in higher organisms and may also be an explanation for the decrease in the relative abundance of certain Flavobacteria at the Normanby seeps (Hassenrück et al. 2016), many of which are known to be aerobic degraders of complex organic compounds.

When oxygen is depleted many microorganisms are able to use alternative electron acceptors, for example, sulfate. However, also sulfate reduction rates were very low at most seep sites. Low sulfate reduction rates are consistent with a decrease in the relative abundance of known sulfate reducers of the

deltaproteobacterial family of Desulfobacteriaceae at these sites (Hassenrück et al. 2016). Sulfate availability did not limit sulfate reduction rates (Supporting Information Fig. S2) and only may become limiting at low millimolar sulfate concentrations (Jørgensen et al. 2019). The moderate increase in temperature in the seep sediments cannot have decreased sulfate reduction. Low pH can reduce sulfate reduction rates (Bayraktarov et al. 2013) and the abundance of sulfate reducers (Sievert et al. 1999). However, our data indicate that low organic matter supply is the main limitation for sulfate reduction. In support of this, sulfate reduction rates decreased with the organic carbon content of the sediments (Fig. 4a,d) and depth, where typically less degradable organic carbon is present. Organic carbon supply as limiting factor is further supported by the higher sulfate reduction rates in seep sediments colonized by seagrass. Despite smallest grain sizes and lowest permeabilities, sulfate reduction rates in seagrass seep sediments were similar or even higher than at the shallow "non-seepage" site. Seagrass is known to fuel sulfate reduction in sediments by supplying organic carbon, for example, through the exudation of organic matter via leaves, roots, and rhizomes (Barrón et al. 2014) and the settling of suspended organic material by reduction of local hydrodynamics by seagrass canopies (Gacia and Duarte 2001). These mechanisms resulted in the highest sedimentary organic carbon content and sulfate reduction rates in the Seagrass site.

Ecological consequences for the reef habitat

Toxic metals, reduction in oxygen and total organic carbon availability can have immediate effects on life in sediments. Nematodes are usually quite resilient to environmental stress (Molari et al. 2018). Our results showed that the abundance of meiofauna and nematodes and the functional diversity of nematodes were reduced in seep sediments (Fig. 4e). This has been attributed to the prevalent environmental conditions, especially low pH and high temperature, in the sediments (Zeppilli and Danovaro 2009; Molari et al. 2018). Whereas the shallow "non-seepage" site was inhabited by small-sized Epsilonematidae and Draconematidae typical for dynamic sediments, only genera exhibiting tolerance to extreme and chronic high pCO_2/low pH conditions are able to exploit the harsh seep sites (e.g., *Oncholaimus*). The species *Oncholaimus campylocercoides* has been frequently reported in seep/venting sites (Zeppilli and Danovaro 2009, Molari et al. 2018). The reduced total organic carbon supply due to decreased permeability implies a reduced food source for meiofauna at seeps. Vice versa the highest abundance of meiofauna and highest functional diversity (feeding types) of nematodes were found in the shallow "non-seepage" site, where organic carbon supply was 2.5 times higher than in the seep sites. The higher food availability (total organic carbon and higher microbial diversity) enabled the selective deposit feeding nematodes to thrive here. Similar to the reduction in functional richness in nematode communities, the microbial communities had a significantly reduced diversity in the seep sediments (Hassenrück et al. 2016). Meiofauna community structure in seeps is thus influenced by the pore water chemistry, reduced supply of organics and by a reduced diversity and density of the microbiota (foodweb effect; Zeppilli and Danovaro 2009). Vice versa, the lower meiofauna abundance in seep sediments may result in a reduced grazing pressure on microorganisms, particularly in deeper sediment layers.

Coastal regions host rich and diverse biological communities and the advection of hydrothermal fluids could be both advantageous and deleterious for the local reef ecosystem above the sediments. Fluxes of metals from the sediments into the overlying water column, including Fe and Mn (Table 2), vary between sediment patches and also with time within one patch, but are overall relatively high, that is, of the same order of magnitude as the oxygen uptake rates by the sediment. Some Fe and Mn likely persist in the fluids as they mix with seawater, because Mn oxidation rates are slow and the relatively low pH will increase the solubility of Fe. Also, complexation of Fe with organic material, as found at shallow-water hydrothermal systems, can prevent oxidation and precipitation of iron (Kleint et al. 2017). Thus, in addition to high CO_2 concentrations and low pH, relatively high concentrations of Fe can be released into the photic zone. This might have positive effects on primary production above the sediment surface as iron can be a limiting or co-limiting micronutrient for phytoplankton in many oceanic surface waters (Nielsdóttir et al. 2012). As the water residence time on the reef is roughly 2.5 h (Smith et al. 2016) and tides have a strong effect on the seepage rates (Fig. 2), we expect fast transport of seep fluids away from the release site. Fe released from shallow-water hydrothermal seeps could also be important, for example, for reef algae (Entsch et al. 1983). Inputs of other metals from the seeps, including Mn, Co, Ni, and As may also affect the coral reef ecosystem. Mn can be a key trace element for coral symbionts and can enhance coral resistance to temperature-induced bleaching (Biscéré et al. 2018). By contrast, increased concentrations of other metals, such as Co and Ni, can decrease coral growth rates (Biscéré et al. 2015, 2017). Although As can be toxic, it was not found to accumulate in coral-inhabited seep sites with high As concentration in the fluids (Pichler et al. 2000).

In addition to the metals, essential nutrients such as NH_4 and Si and occasionally PO_4 were present in the pore waters of Normanby Island seep sediments and will be advected into the water column. Comparing areal release rates with literature values of nutrient uptake in coral reefs (Webb et al. 1975; Steven and Atkinson 2003), the amount of NH_4 released from the seep sites was on average 6 mmol m^{-2} d^{-1}, which is close to natural turnover of N in coral reefs (– 1 to 7.8 mmol m^{-2} d^{-1}). Similarly, average phosphate input into the ecosystem from the sediment patches (~ 0.3 mmol m^{-2} d^{-1}) was comparable to the range for natural phosphate cycling (0.35–3.8 mmol m^{-2} d^{-1}). Hence nutrient inputs from seeps might

be beneficial to the reef environment. Due to its high concentration in the hydrothermal fluids, the average Si flux from the seep sediments (125 mmol m^{-2} d^{-1}) was nearly 85 times higher than the highest flux we have found from coral reef sediments in the literature (– 0.02 to 1.5 mmol m^{-2} d^{-1}, Ullman and Sandstrom 1987). Increased Si supply from shallow-water hydrothermal seeps could thus stimulate the growth of silicate incorporating organisms like diatoms and sponges. Total release rates from the seepage area were 2.1 mol d^{-1} NH_4, 0.1 mol d^{-1} PO_4, and 45 mol d^{-1} Si.

Conclusions

Shallow-water hydrothermal seeps, such as offshore Normanby Island, are extreme environments with unique biogeochemical conditions originating from the advection of CO_2- and metal-rich fluids. The geochemistry of pore waters and sediments around the hydrothermal seeps is strongly affected by the hydrothermal fluids, but also by reactions between the fluids and the sediments, organic matter degradation and precipitation of redox reactive metals. We have shown that the quantities of nutrients released from the sediment into the water column are sufficient to have an effect on the ecosystem, as they are comparable to or even higher than natural turnover rates in coral reefs. These fluxes could have positive, albeit local, effects on the pelagic ecosystem. In the sediments, by contrast, the advection of hydrothermal fluids has negative effects on the benthic environment, changing the community structure and the efficiency of carbon degradation. This occurs either directly, through the accumulation of toxic metals and through decalcification, or indirectly through a decreased supply of organic carbon and oxygen into the sediments due to changes in sediment permeability.

References

Ahmerkamp, S., H. K. Marchant, C. Peng, D. Probandt, S. Littmann, M. M. Kuypers, and M. Holtappels. 2020. The effect of sediment grain properties and porewater flow on microbial abundance and respiration in permeable sediments. Sci. Rep. **10**: 1–12. doi:10.1038/s41598-020-60557-7

Aiuppa, A., J. M. Hall-Spencer, M. Milazzo, G. Turco, S. Caliro, and R. Di Napoli. 2021. Volcanic CO_2 seep geochemistry and use in understanding ocean acidification. Biogeochem. **152**: 93–115. doi:10.1007/s10533-020-00737-9

Barrón, C., E. T. Apostolaki, and C. M. Duarte. 2014. Dissolved organic carbon fluxes by seagrass meadows and macroalgal beds. Mar. Biogeochem. **1**: 42. doi:10.3389/fmars.2014.00042

Bayraktarov, E., R. E. Price, T. G. Ferdelman, and K. Finster. 2013. The pH and pCO_2 dependence of sulfate reduction in shallow-sea hydrothermal CO_2—Venting sediments (Milos Island, Greece). Extreme Microbiol. **4**: 111. doi:10.3389/fmicb.2013.00111

Biscéré, T., R. Rodolfo-Metalpa, A. Lorrain, L. Chauvaud, J. Thébault, J. Clavier, and F. Houlbrèque. 2015. Responses of two scleractinian corals to cobalt pollution and ocean acidification. PLoS One **10**: 1–18. doi:10.1371/journal.pone.0122898

Biscéré, T., and others. 2017. Nickel and ocean warming affect scleractinian coral growth. Mar. Pollut. Bull. **120**: 250–258. doi:10.1016/j.marpolbul.2017.05.025

Biscéré, T., C. Ferrier-Pagès, A. Gilbert, T. Pichler, and F. Houlbrèque. 2018. Evidence for mitigation of coral bleaching by manganese. Sci. Rep. **8**: 1–10.

Bischoff, J. L., and W. E. Seyfried. 1978. Hydrothermal chemistry of seawater from 25 degrees to 350 degrees C. Am. J. Sci. **278**: 838–860. doi:10.2475/ajs.278.6.838

Butterfield, D. A., G. J. Massoth, R. E. McDuff, J. E. Lupton, and M. D. Lilley. 1990. Geochemistry of hydrothermal fluids from Axial Seamount hydrothermal emissions study vent field, Juan de Fuca Ridge: Subseafloor boiling and subsequent fluid-rock interaction. J. Geophys. Res. Solid Earth **95**: 12895–12921. doi:10.1029/JB095iB08p12895

Cline, J. D. 1969. Spectrophotometric determination of hydrogen sulfide in natural waters. Limnol. Oceanogr. **14**: 454–458. doi:10.4319/lo.1969.14.3.0454

de Beer, D., and others. 2005. Transport and mineralization rates in North Sea sandy intertidal sediments, Sylt-Rømø Basin, Wadden Sea. Limnol. Oceanogr. **50**: 113–127. doi:10.4319/lo.2005.50.1.0113

de Beer, D., M. Haeckel, J. Neumann, G. Wegener, F. Inagaki, and A. Boetius. 2013. Saturated CO_2 inhibits microbial processes in CO_2-vented deep-sea sediments. Biogeosciences **10**: 5639–5649. doi:10.5194/bg-10-5639-2013

Entsch, B., R. G. Sim, and B. G. Hatcher. 1983. Indications from photosynthetic components that iron is a limiting nutrient in primary producers on coral reefs. Mar. Biol. **73**: 17–30. doi:10.1007/BF00396281

Fabricius, K. E., and others. 2011. Losers and winners in coral reefs acclimatized to elevated carbon dioxide concentrations. Nature Clim. Change **1**: 165–169. doi:10.1038/nclimate1122

Flohr, A., J. M. Matter, R. H. James, K. Saw, R. Brown, J. Gros, and others. 2021. Utility of natural and artificial geochemical tracers for leakage monitoring and quantification during an offshore controlled CO_2 release experiment. Int. J. Greenhouse Gas Control **111**: 103421.

Gacia, E., and C. M. Duarte. 2001. Sediment retention by a Mediterranean Posidonia oceanica meadow: The balance between deposition and resuspension. Estuar. Coast. Shelf Sci. **52**: 505–514. doi:10.1006/ecss.2000.0753

Grevemeyer, I., N. Kaul, and J. L. Diaz-Naveas. 2006. Geothermal evidence for fluid flow through the gas hydrate stability field off Central Chile—Transient flow related to large subduction zone earthquakes? Geophys. J. Int. **166**: 461–468. doi:10.1111/j.1365-246X.2006.02940.x

Guilini, K. and others (2016). NeMys: world database of free-living marine nematodes. Available online at: http://nemys.ugent.be

Haeckel, M., B. P. Boudreau, and K. Wallmann. 2007. Bubble-induced porewater mixing: A 3-D model for deep porewater irrigation. Geochim. Cosmochim. Acta **71**: 5135–5154. doi:10.1016/j.gca.2007.08.011

Hall-Spencer, and others. 2008. Volcanic carbon dioxide vents show ecosystem effects of ocean acidification. Nature **454**: 96–99. doi:10.1038/nature07051

Hassenrück, C., A. Fink, A. Lichtschlag, H. E. Tegetmeyer, D. de Beer, and A. Ramette. 2016. Quantification of the effects of ocean acidification on sediment microbial communities in the environment: The importance of ecosystem approaches. FEMS Microbiol. Ecol. **fiw027**.

Heip, C., Vincx, M., & Vranken, G. 1985. The ecology of marine nematodes. 399-489.

Huettel, M., P. Cook, F. Janssen, G. Lavik, and J. J. Middelburg. 2007. Transport and degradation of a dinoflagellate bloom in permeable sublittoral sediment. Mar. Ecol. Prog. Ser. **340**: 139–153. doi:10.3354/meps340139

James, R. H., D. E. Allen, and W. E. Seyfried. 2003. An experimental study of alteration of oceanic crust and terrigenous sediments at moderate temperatures (51 to 350°C): Insights as to chemical processes in near-shore ridge-flank hydrothermal systems. Geochim. Cosmochim. Acta **67**: 681–691. doi:10.1016/S0016-7037(02)01113-4

Jørgensen, B. B. 1978. A comparison of methods for the quantification of bacterial sulfate reduction in coastal marine sediments: I. Measurement with radiotracer techniques. Geomicrobiol. J. **1**: 11–27.

Jørgensen, B. B., and A. Boetius. 2007. Feast and famine—Microbial life in the deep-sea bed. Nat. Rev. Microbiol. **5**: 770–781. doi:10.1038/nrmicro1745

Jørgensen, B. B., A. J. Findlay, and A. Pellerin. 2019. The biogeochemical sulfur cycle of marine sediments. Front. Microbiol. **10**: 849.

Kelly, D. And C. Richards. 2018. oce: Analysis of oceanographic data. R package version 0.9-23. Available from https://CRAN.R-project.org/package=oce"

Kleint, C., T. Pichler, and A. Koschinsky. 2017. Geochemical characteristics, speciation and size-fractionation of iron (Fe) in two marine shallow-water hydrothermal systems, Dominica, Lesser Antilles. Chem. Geol. **454**: 44–53. doi:10.1016/j.chemgeo.2017.02.021

Kostka, J. E., and G. W. Luther III. 1994. Partitioning and speciation of solid phase iron in saltmarsh sediments. Geochim. Cosmochim. Acta **58**: 1701–1710. doi:10.1016/0016-7037(94)90531-2

Larsen, M., S. M. Borisov, B. Grunwald, I. Klimant, and R. N. Glud. 2011. A simple and inexpensive high resolution color ratiometric planar optode imaging approach: Application to oxygen and pH sensing. Limnol. Oceanogr. Methods **9**: 348–360. doi:10.4319/lom.2011.9.348

Long, E., D. Macdonald, S. Smith, and F. Calder. 1995. Incidence of adverse biological effects within ranges of chemical concentrations in marine and estuarine sediments. Environ. Manag. **19**: 81–97. doi:10.1007/BF02472006

Martins, M., and others. 2021. Ervilia castanea (Mollusca, Bivalvia) populations adversely affected at CO_2 seeps in the North Atlantic. Sci. Total Environ. **754**: 142044. doi:10.1016/j.scitotenv.2020.142044

Mokadem, F., I. J. Parkinson, E. C. Hathorne, P. Anand, J. T. Allen, and K. W. Burton. 2015. High-precision radiogenic strontium isotope measurements of the modern and glacial ocean: Limits on glacial–interglacial variations in continental weathering, Earth Planet. Sci. Lett. **415**: 111–120.

Molari, M., and others. 2018. CO_2 leakage alters biogeochemical and ecological functions of submarine sands. Sci. Adv. **4**: eaao2040. doi:10.1126/sciadv.aao2040

Nielsdóttir, M. C., T. S. Bibby, C. M. Moore, D. J. Hinz, R. Sanders, M. Whitehouse, R. Korb, and E. P. Achterberg. 2012. Seasonal and spatial dynamics of iron availability in the Scotia Sea. Mar. Chem. **130**: 62–72.

Oksanen, J. and others, 2019. vegan: community ecology package. R package version 2.5-6.2019.

Pichler, T., J. Veizer, and G. E. M. Hall. 1999*a*. The chemical composition of shallow-water hydrothermal fluids in Tutum Bay, Ambitle Island, Papua New Guinea and their effect on ambient seawater. Mar. Chem. **64**: 229–252.

Pichler, T., J. A. N. Veizer, and G. E. Hall. 1999*b*. Natural input of arsenic into a coral-reef ecosystem by hydrothermal fluids and its removal by Fe (III) oxyhydroxides. Environ. Sci. Technol. **33**: 1373–1378.

Pichler, T., J. M. Heikoop, M. J. Risk, J. Veizer, and I. L. Campbell. 2000. Hydrothermal effects on isotope and trace element records in modern reef corals: A study of Porites lobata from Tutum Bay, Ambitle Island, Papua New Guinea. Palaios **15**: 225–234. doi:10.2307/3515644

Polerecky, L., U. Franke, U. Werner, B. Grunwald, and D. de Beer. 2005. High spatial resolution measurement of oxygen consumption rates in permeable sediments. Limnol. Oceangr. Methods **3**: 75–85.

Poulton, S. W., and D. E. Canfield. 2006. Co-diagenesis of iron and phosphorus in hydrothermal sediments from the southern East Pacific Rise: Implications for the evaluation of paleoseawater phosphate concentrations. Geochim. Cosmochim. Acta **70**: 5883–5898. doi:10.1016/j.gca.2006.01.030

R Core Team. 2020. R: A language and environment for statistical computing. R Foundation for Statistical Computing, . Available from https://www.R-project.org/, DOI: 10.21873/invivo.12201.

Rasheed, M., M. I. Badran, C. Richter, and M. Huettel. 2002. Effect of reef framework and bottom sediment on nutrient enrichment in a coral reef of the Gulf of Aqaba, Red Sea. Mar. Ecol. Prog. Ser. **239**: 277–285. doi:10.3354/meps239277

Resing, J. A., P. N. Sedwick, C. R. German, W. J. Jenkins, J. W. Moffett, B. M. Sohst, and A. Tagliabue. 2015. Basin-scale transport of hydrothermal dissolved metals across the South Pacific Ocean. Nature **523**: 200–203. doi:10.1038/nature14577

Revsbech, N. P. 1989. An oxygen microsensor with a guard cathode. Limnol. Oceanogr. **34**: 474–478. doi:10.4319/lo.1989.34.2.0474

Røy, H., H. S. Weber, I. H. Tarpgaard, T. G. Ferdelman, and B. B. Jørgensen. 2014. Determination of dissimilatory sulfate reduction rates in marine sediment via radioactive ^{35}S tracer. Limnol. Oceanogr. Methods **12**: 196–211. doi:10.4319/lom.2014.12.196

Sedwick, P., and D. Stueben. 1996. Chemistry of shallow submarine warm springs in an arc-volcanic setting: Vulcano Island, Aeolian Archipelago. Italy Mar. Chem. **53**: 147–161. doi:10.1016/0304-4203(96)00020-5

Seinhorst, J. W. 1959. A rapid method for the transfer of nematodes from fixative to anhydrous glycerin. Nematologica **4**: 67–69. doi:10.1163/187529259X00381

Sievert, S. M., T. Brinkhoff, G. Muyzer, W. Ziebis, and J. Kuever. 1999. Spatial heterogeneity of bacterial populations along an environmental gradient at a shallow submarine hydrothermal vent near Milos Island (Greece). Appl. Environ. Microbiol. **65**: 3834–3842. doi:10.1128/AEM.65.9.3834-3842.1999

Smith, I. E. M., and W. Compston. 1982. Strontium isotopes in Cenozoic volcanic rocks from southeastern Papua New Guinea. Lithos **15**: 199–206. doi:10.1016/0024-4937(82)90011-1

Smith, J. N., G. De'ath, C. Richter, A. Cornils, J. M. Hall-Spencer, and K. E. Fabricius. 2016. Ocean acidification reduces demersal zooplankton that reside in tropical coral reefs. Nature Clim. Change **6**: 1124–1129. doi:10.1038/nclimate3122

Steven, A. D. L., and M. J. Atkinson. 2003. Nutrient uptake by coral-reef microatolls. Coral Reefs **22**: 197–204. doi:10.1007/s00338-003-0303-8

Ullman, W. J., and M. W. Sandstrom. 1987. Dissolved nutrient fluxes from the nearshore sediments of Bowling Green Bay, central Great Barrier Reef lagoon (Australia). Estuar. Coast. Shelf Sci. **24**: 289–303. doi:10.1016/0272-7714(87)90051-5

Viollier, E., P. W. Inglett, K. Hunter, A. N. Roychoudhury, and P. Van Cappellen. 2000. The ferrozine method revisited: Fe (II)/Fe (III) determination in natural waters. Appl. Geochem. **15**: 785–790. doi:10.1016/S0883-2927(99)00097-9

Vizzini, S., R. Di Leonardo, V. Costa, C. D. Tramati, F. Luzzu, and A. Mazzola. 2013. Trace element bias in the use of CO_2 vents as analogues for low pH environments: Implications for contamination levels in acidified oceans. Estuar. Coast. Shelf Sci. **134**: 19–30. doi:10.1016/j.ecss.2013.09.015

Von Damm, K. L. 2001. Chemistry of hydrothermal vent fluids. *In* J. Kirk Cochran, H. J. Bokuniewicz, and P. L. Yager [eds.], 1246–1253. Encyclopedia of ocean sciences. Academic Press. San Diego

Webb, K. L., W. D. DuPaul, W. Wiebe, W. Sottile, and R. E. Johannes. 1975. Enewetak (Eniwetok) Atoll: Aspects of the nitrogen cycle on a coral reef. Limnol. Oceanogr. **20**: 198–210. doi:10.4319/lo.1975.20.2.0198

Wenzhöfer, F., O. Holby, R. N. Glud, H. K. Nielsen, and J. K. Gundersen. 2000. In situ microsensor studies of a shallow water hydrothermal vent at Milos. Greece. Mar. Chem. **69**: 43–54. doi:10.1016/S0304-4203(99)00091-2

Werner, U., P. Bird, C. Wild, T. Ferdelman, L. Polerecky, G. Eickert, R. Jonstone, O. Hoegh-Guldberg, and D. de Beer. 2006. Spatial patterns of aerobic and anaerobic mineralization rates and oxygen penetration dynamics in coral reef sediments. Mar. Ecol. Prog. Ser. **309**: 93–105. doi:10.3354/meps309093

Werner, U., A. Blazejak, P. Bird, G. Eickert, R. Schoon, R. M. M. Abed, A. Bissett, and D. de Beer. 2008. Microbial photosynthesis in coral reef sediments (Heron Reef, Australia). Estuar. Coast. Shelf Sci. **76**: 876–888. doi:10.1016/j.ecss.2007.08.015

Wheat, C. G., R. A. Feely, and M. J. Mottl. 1996. Phosphate removal by oceanic hydrothermal processes: An update of the phosphorus budget in the oceans. Geochim. Cosmochim. Acta **60**: 3593–3608. doi:10.1016/0016-7037(96)00189-5

Wieser, W. 1953. Die Beziehung zwischen Mundhoehlengestalt, Emaehrungsweise und Vorkommen bei freilebenden Wieser, W. Kanwisher, J. (1961). Ecological and physiologimarinen Nematoden. Arkiv. Zool. **4**: 439484.

Zeppilli, D., and R. Danovaro. 2009. Meiofaunal diversity and assemblage structure in a shallow-water hydrothermal vent in the Pacific Ocean. Aquat. Biol. **5**: 75–84. doi:10.3354/ab00140

Acknowledgments

We thank the owners of Upa-Upasina reef for allowing our work. We are grateful to captain Rob van de Loos and the wonderful crew of the MS Chertan for assistance on board and in the field. We thank all participants of the cruises to Papua New Guinea, especially Katharina Fabricius for her support in organization and sharing her knowledge of this site and Karin Hohmann for help during the cruise. Artur Fink, Ambra Milani, Cathy Cole, Richard Pearce and Matt Cooper are gratefully acknowledged for their assistance in the laboratory. We also thank Sergey Borisov from the University of Graz for providing the oxygen optode foils. This study was financially supported by the German Ministry for Research and Education (BMBF) project on the Biological Impacts of Ocean Acidification (BIOACID II, grant no. FKZ 03F0655C) and the Max Planck Society. U.B. is a senior postdoctoral research fellow at Research Foundation—Flanders (FWO Belgium, grant no. 1201720 N).

Submitted 12 April 2021
Revised 22 September 2021
Accepted 14 December 2021

Associate editor: Vanessa Hatje